Supplementary Information

Selective Induction of Optical Magnetism

Uttam Manna[1,#,$], Jung–Hoon Lee[2,$], Tian–Song Deng[2,$], John Parker[1,3,$], Nolan Shepherd[1,2], Yossi Weizmann[2], Norbert F. Scherer[1,2,1]

[1]The James Franck Institute, [2]Department of Chemistry, [3]Department of Physics, University of Chicago, Chicago, IL 60637, USA

[#] Present Address: Department of Physics, Illinois State University, Normal, IL 61790, USA
[$] These authors contributed equally to this work.
[1]Email: nfschere@uchicago.edu

Creation and Characterization of Cylindrical Vector Beams (CVBs). For the present experiments, we use a liquid-crystal (LC) based polarization converter (from ARCoptix) that uses twisted nematic liquid crystals sandwiched between one uniform and one circularly rubbed alignment layer to generate azimuthally and radially polarized CVBs[1]. The polarization-guiding effect in this LC based device is valid for $\pi d\Delta n/\chi >> \lambda$, where Δn is the birefringence of the LC, d is the cell thickness, χ is the twist angle of the LC, and λ is the wavelength of the incident light[1]. For high $d\Delta n$, the polarization reorientation effect is valid over a broad wavelength range – hence, the polarization converter can be utilized to produce broadband CVBs, provided that the wavelength-dependent phase difference of the retarder used to eliminate the phase difference in two halves of the LC device is accounted for. A schematic of the vector beam spectroscopy and microscopy set-up is shown in Fig. S1b. We use a spatially (but not temporally) coherent (broadband) white light continuum (400-2700 nm) for our spectroscopic measurements. The white light continuum is coupled to an inverted optical microscope (Olympus IX-81) equipped with a 100X oil immersion objective with numerical aperture NA = 1.4 (Olympus SAPO). The vector beam generator was placed just before the microscope objective. The beam quality was monitored in the forward direction using an objective and tubelens (not shown in Fig. 1). The back-scattered images of the sample plane were recorded by a sCMOS array detector (Andor Neo) connected to the trinoc eye-piece of the microscope and spectra acquired by an EM-CCD (Andor Newton) connected to an imaging spectrometer coupled to the side port of the microscope via a home-built achromatic 4*f* relay system.

Fig. S1c shows the images of the broadband azimuthally and radially polarized beams that were generated experimentally, and detected in transmission. The spatial orthogonality of the polarizations associated with the azimuthal and radial beams were detected by inserting a linear polarizer in front of the array detector at different angles as shown in Fig. S1c.

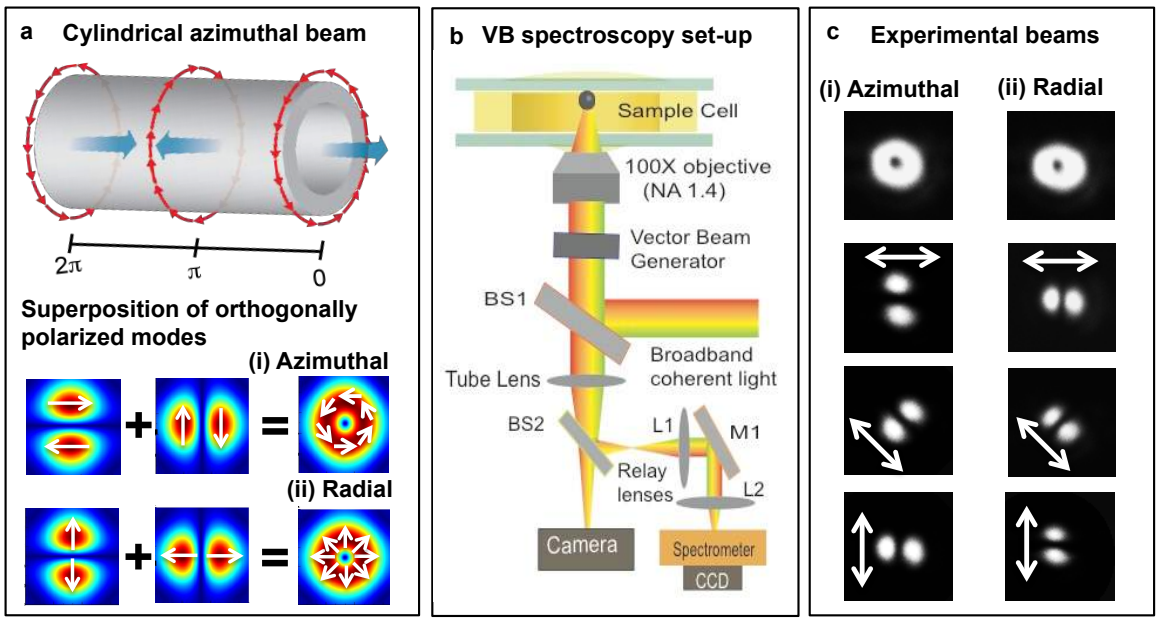

Figure S1. Generation of broadband CVBs. (**a**) Schematic representation of CVBs with right- and left-handed azimuthal polarization; and the superposition of orthogonally polarized HG_{01} and HG_{10} modes forming azimuthal and radial CVBs. (**b**) Schematic of the CVB spectroscopy and microscopy set-up. BS, partially reflecting or movable Beam Splitter; L, Lenses; M, Mirror. (**c**) Experimental generation of broadband CVBs with azimuthal and radial polarization and their linear components as determined by inserting a linear polarization analyzer in front of the detector, and measuring the beam in the forward direction (optics not shown).

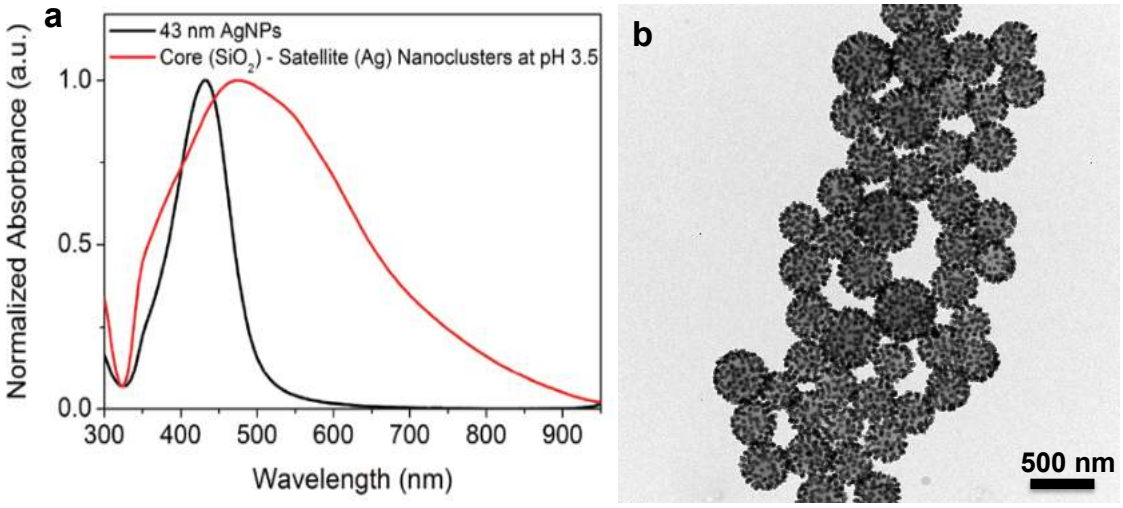

Figure S2. (**a**) The ensemble UV-VIS spectra and (**b**) their associated TEM images of core (300 nm SiO_2) – satellite (43 nm Ag nanoparticles) nano-clusters at pH 3.5.

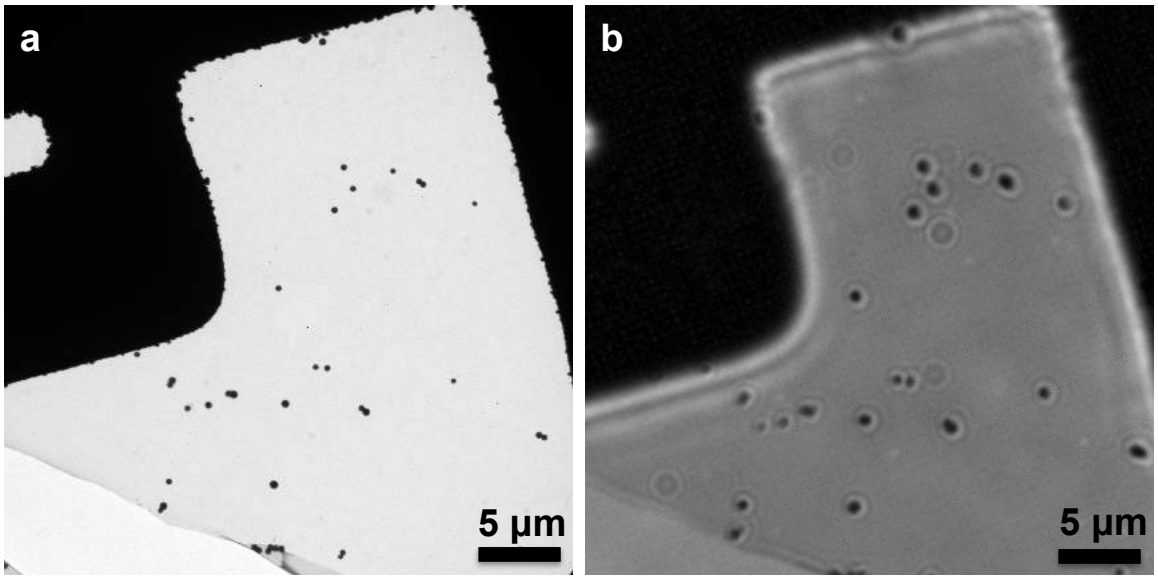

Figure S3. The same area of an EM finder grid imaged by TEM (**a**) and an optical microscope (**b**). Thus we can do single particle spectroscopy, which allows relating the nanostructure and scattering spectra of individual nano-clusters. Note that we assumed that the nano-clusters need to be well separated (~5 µm or more), to avoid any possibility of scattering from multipole clusters that could affect the optical microscopy imaging and the spectra measurement.

Selective excitation of magnetic and electric modes with CVBs. Figures S4-S6 and Figures 2-5 of the main text show experimental and simulation results demonstrating that azimuthally and radially polarized light can selectively excite pure magnetic and electric multipolar modes, respectively, in core-satellite dielectric-metal nano-clusters. Thus spectroscopy with cylindrical vector beams yields more selective and simple spectra than scalar beams (e.g. linearly polarized light) and is thus a powerful approach to probe electric and magnetic modes (dipole, quadrupole, octupole) in a range of optical-meta and photonic materials. Such measurements of electric and magnetic modes in individual nano-clusters are essential in aiding the design and optimization of synthesis of nano-meta-material building blocks, "meta-atoms" that could be assembled to create dense monolayer or multilayer films on substrates and meta-fluids.

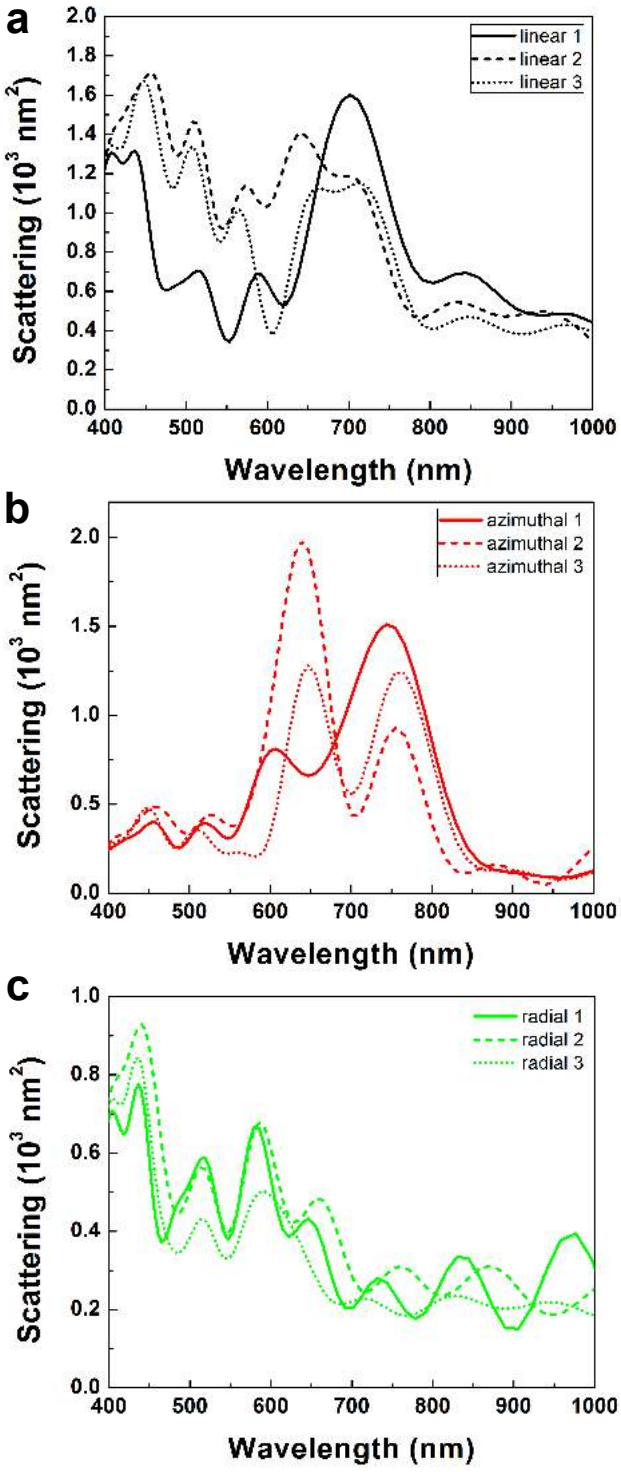

Figure S4. FDTD simulated scattering spectra of a 360 nm core-satellite nano-cluster with three different permutations: permutation 1 (black), permutation 2 (red), and permutation 3 (green). For comparison, we drew separately in (a) linear, (b) azimuthal, and (c) radial. The details of the spectra can change even just with a permutation of the AgNP arrangements even at constant AgNP number on the same core.

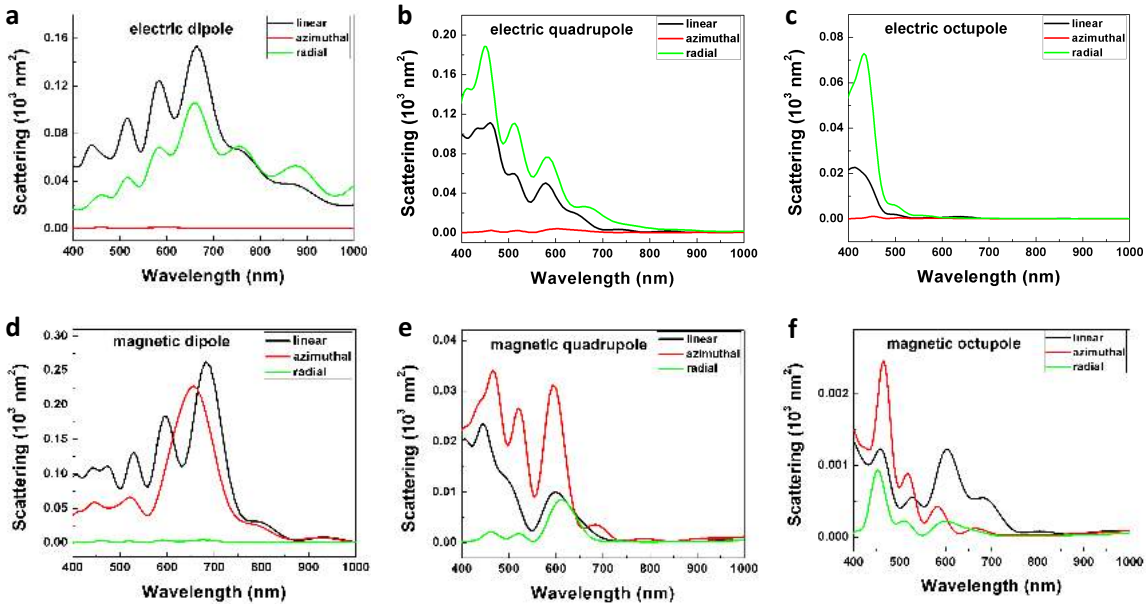

Figure S5. Comparison of the results of multipole expansion of the NC_D165nm nano-cluster excited by three different polarization beams: linear (black), azimuthal (red), and radial (green), respectively. (a) electric dipole, (b) electric quadrupole, (c) electric octupole, (d) magnetic dipole, (e) magnetic quadrupole, (f) magnetic octupole. The TEM result, experimental spectra and simulated spectra should be compared with the results shown in Figures 2 and 3 in the main text.

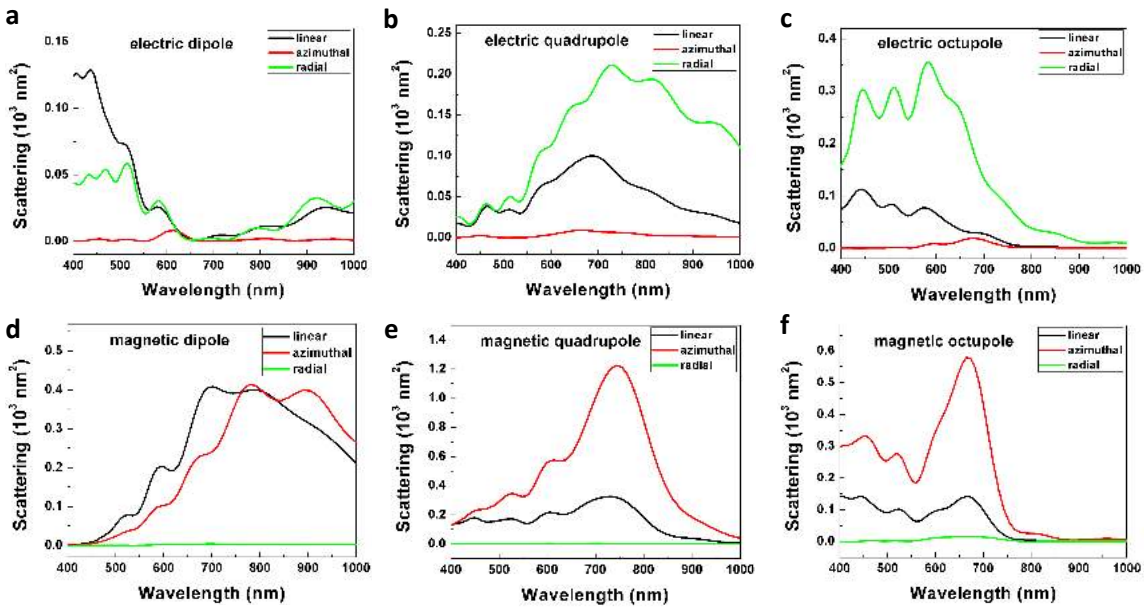

Figure S6. Comparison of the results of multipole expansion of the NC_D360nm nano-cluster excited by three different polarization beams: linear (black), azimuthal (red), and radial (green), respectively. (a) electric dipole, (b) electric quadrupole, (c) electric octupole, (d) magnetic dipole, (e) magnetic quadrupole, (f) magnetic octupole.

Multipole expansion analysis of experimental scattering spectra. In order to compare the experimental scattering spectra from the core-satellite nano-clusters to the FDTD simulated results, the experimental spectra could each be modeled as a sum of Gaussian curves with the functional form

$$f(\lambda) = \sum_{i}^{n} a_i e^{-\frac{(x-x_i)^2}{2\sigma_i^2}}$$

by using nonlinear least-squares fitting after smoothing by Tikhonov regularization. However, when compared to the simulated multipole expansion spectra, it becomes clear that the various multipoles are not well described by these individual peaks. This is in sharp contrast to spectra of metallic spheres calculated by Mie theory, where each peak can be assigned to a certain electric multipolar mode; the multipole expansions of the nano-cluster scattering have numerous peaks each and overlap with each other, as shown in Figure 3.

For a better comparison, the multipole expansion modes from the simulation were considered as a set of 'basis functions'. Expanding the experimental spectra in terms of overlap integrals with the multipoles as a basis highlights the character of the vector beam scattering from the nano-clusters. The smoothed experimental spectra were normalized according to the integral over the wavelength window of the original measurement,

$$\bar{f}(\lambda) = \frac{f(\lambda)}{N_e},\ N_e = \int_{\lambda=500\ nm}^{\lambda=1000\ nm} f(\lambda)\, d\lambda$$

Each of the multipole expansion spectra from the FDTD simulated results were also normalized, but by the integral over the full simulated spectra:

$$\bar{s}_i(\lambda) = \frac{s_i(\lambda)}{N_s},\ i = eD,\ mD,\ eQ,\ mQ,\ \ldots,\ N_s = \int_{\lambda=500\ nm}^{\lambda=1000\ nm} \left(\sum_i s_i(\lambda)\right) d\lambda$$

The overlap between the experimental spectra and each of the multipole expansions was then calculated by the integral

$$O_i = \int_{\lambda=500\ nm}^{\lambda=1000\ nm} \bar{f}(\lambda) * \bar{s}_i(\lambda)\, d\lambda$$

For the example of the scattering of the linearly polarized beam from the 165 nm nanocluster, the spectra had the highest overlap coefficient (O_i) with the electric and magnetic expansions of the simulated spectra (see Figure S7).

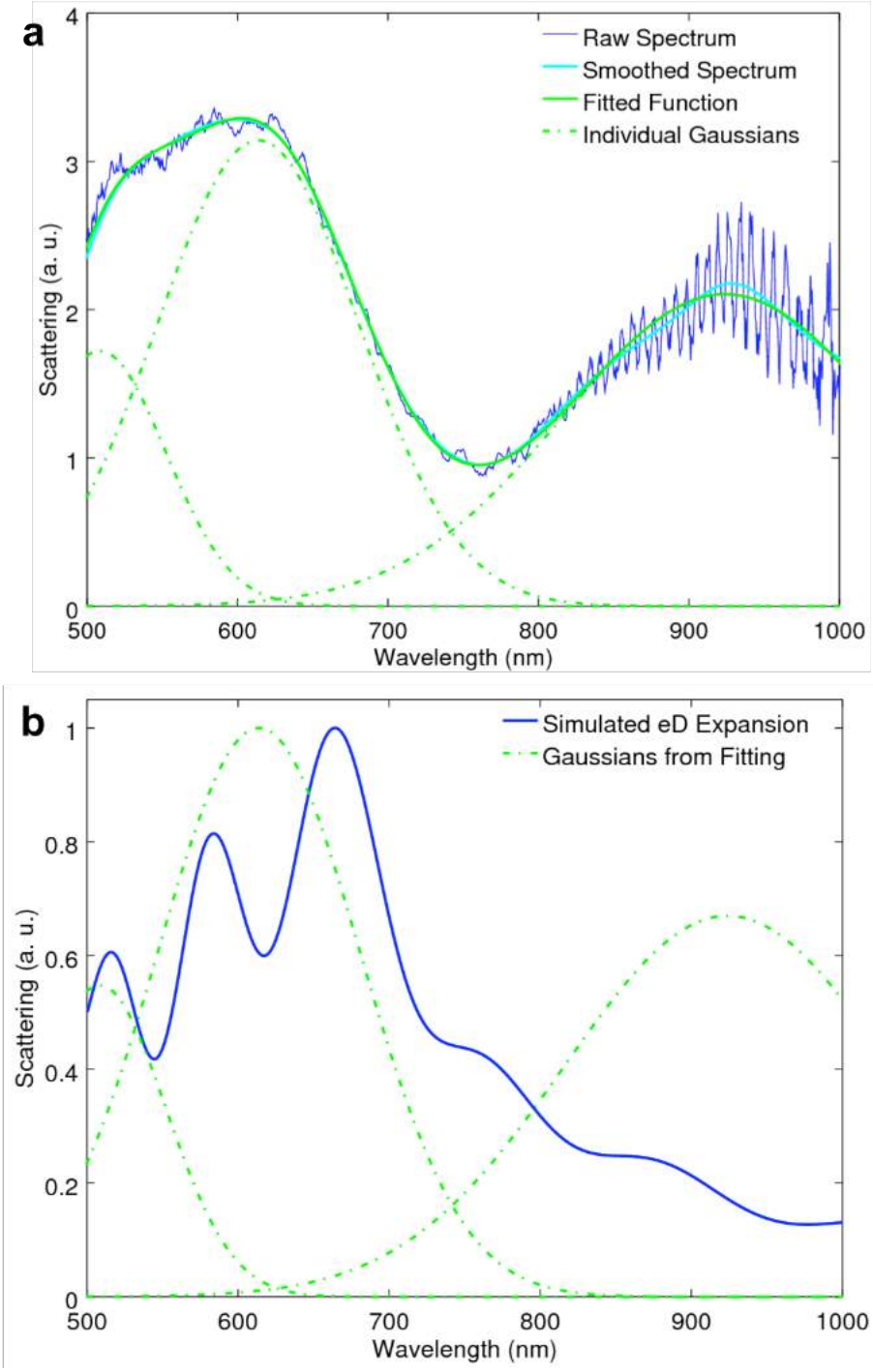

Figure S7. Multipole expansion analysis of experimental scattering spectra. (a) Experimental scattering spectrum of linear beam of 165 nm core-satellite nano-cluster with fit to sum of Gaussians function. The dashed green lines show the individual Gaussian curves that are summed together to form the function for the fitting. (b) Comparison of the individual Gaussian curves from the fit to the experimental linear scattering spectrum to the electric dipole expansion of the simulated linear scattering spectrum.

FDTD Simulations. FDTD simulations with small mesh sizes of short chians of 2-4 AgNPs with small spacings were carried out with commercial software Lumerical FDTD Solutions 8.18. A total-field scattered-field source was used to simulate a propagating plane wave interacting with the AgNP chains, with a wavelength range of 600 to 1000 nm. Only longitudial surface plasmon resonance was calculated by setting the excitation polarization along the axis of the chains. A three-dimensional nonuniform mesh was used, and a grid size of 1.0-0.4 nm was chosen for the AgNP chains. The size of Ag nanoparticles is 40 nm in diameter. We simulated chains with 2-4 AgNPs and their gaps/grid sizes are set as 1.0 nm, 0.8 nm, 0.6 nm, and 0.4 nm respectively. The results are shown in Figure S8.

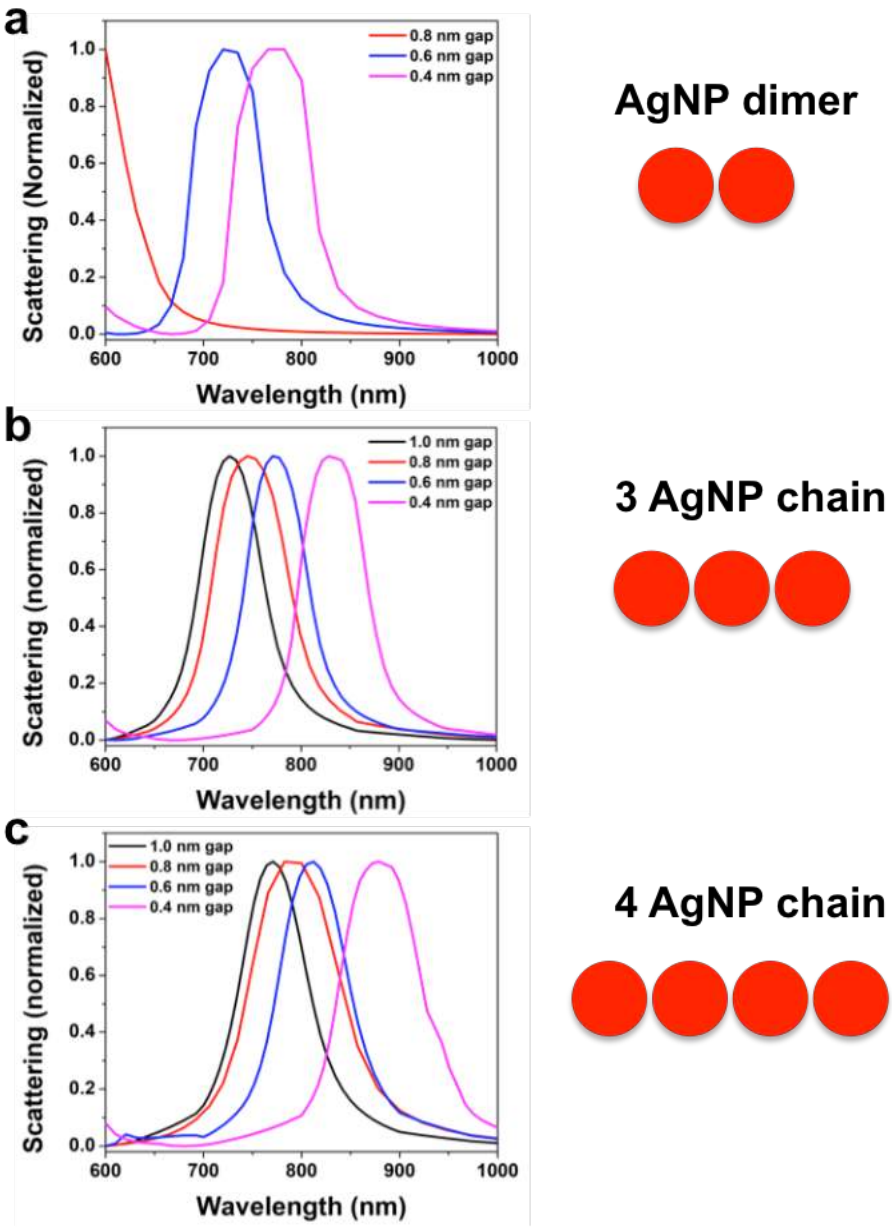

Figure S8. FDTD simulations of AgNP chains with sub-nanometer gaps excited by linear polarization parallel to the chain axis. (a) Scattering cross section of AgNP dimer with gaps of 0.8 nm, 0.6 nm, and 0.4 nm; (b) Scattering cross section of 3-AgNP chain with gaps of 1.0 nm, 0.8 nm, 0.6 nm, and 0.4 nm; and (c) Scattering cross section of 4-AgNP chain with gaps of 1.0 nm, 0.8 nm, 0.6 nm, and 0.4 nm. The plasmonic resonances red-shift with increasing of the number of Ag nanoparticles and/or decreasing the gaps between Ag nanoparticles.

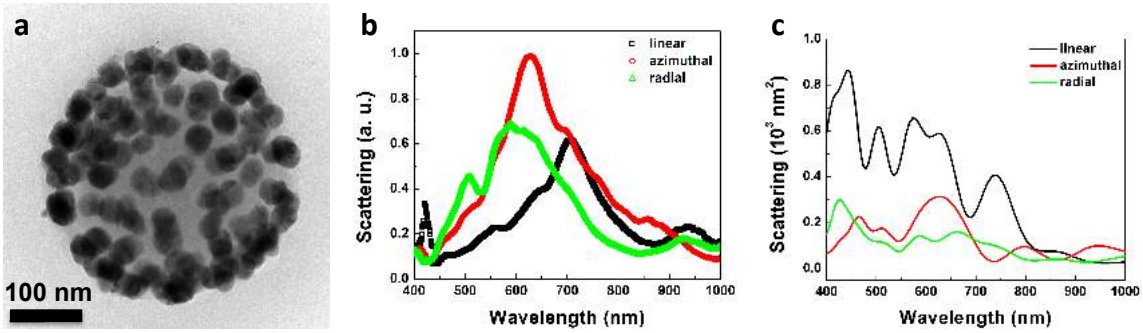

Figure S9. TEM image (a), experimental (b) and simulated scattering spectra (c) of core-satellite nano-cluster with SiO_2 core size of 280 nm, and Ag nanoparticles size of 43 nm. Note here the density of AgNPs is lower than that of the NC_D360nm nano-cluster.

Excitation of magnetic mode with scalar beams vs. vector beams. Excitation of magnetic modes with linearly polarized light in core-satellite nano-clusters relies on the breaking of perfect cylindrical symmetry of the arrangements of the metal nanoparticles and/or retardation[2-4]. Therefore, structural defects or irregularities allow excitation of net displacement currents. Our simulated spectra (Figures S4-S6, Figures 2-5 of the main text) and displacement currents (Figure S10) show that these modes are not identical to those created with azimuthally polarized light. The the magnetic modes excited with linearly polarized light rely on broken symmetry and retardation while the magnetic modes excited with azimuthally polarized CVBs only require close poximimity and coupling of the metal nanoparticles to allow driving a displacement current that subtends (most of) the circumference (i.e. along longitudinal loops) of the core-satellite structure.

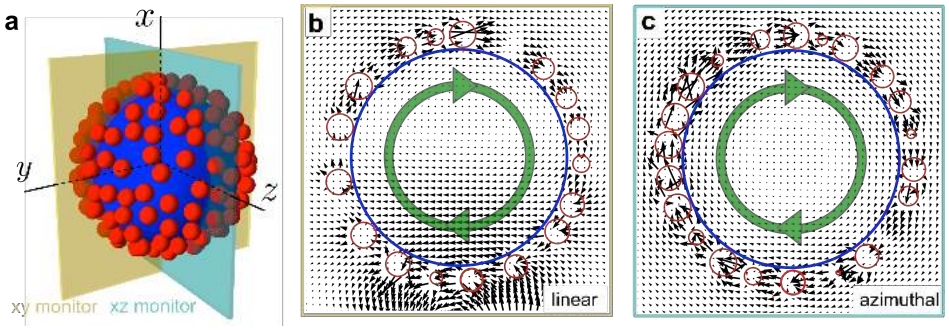

Figure S10. Magnetic moments arising from excitation with linearly polarized light and azimuthally polarized CVBs. (a) The coordinate system and xz and xy planes cutting through a core-satellite structure used in FDTD simulations. (b) Displacement currents in the xz plane created with linearly polarized light. (c) Displacement currents in the xy plane created with azimuthally polarized CVBs.

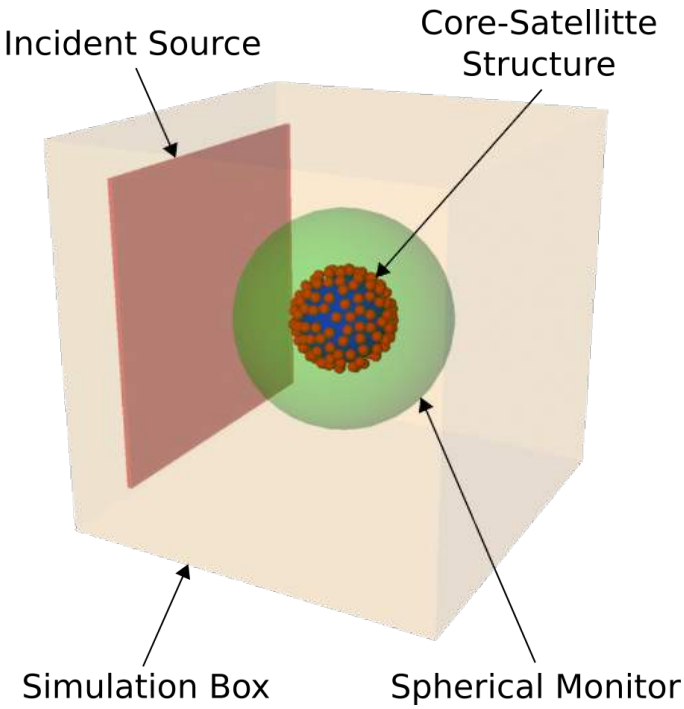

Figure S11. The simulation setup. A source is propagated from the red plane. The core-satellite structure is placed at the center of the simulation box. A 50 nm (25 cell) thick perfectly matched layer (PML) is used as the boundary condition. The green sphere surrounding the core-satellite structure is a special spherical monitor that collects the scattered electric field, including magnitude, polarization and phase information. The data collected from this monitor is used in the multipole expansion.

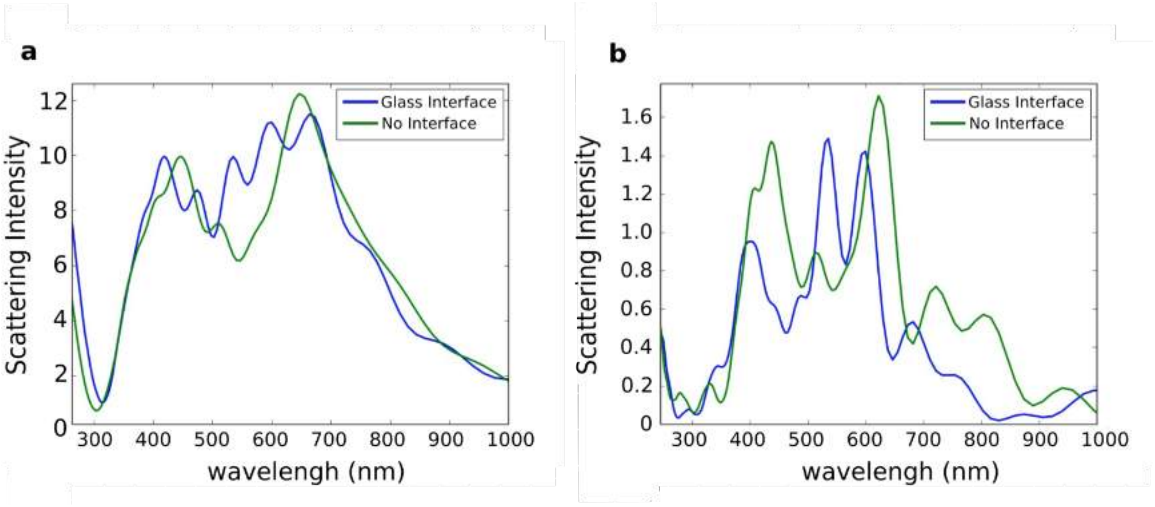

Figure S12. Simulation results of a core-satellite structure immersed in water and resting on a glass interface. The incident source is a linearly polarized Gaussian beam. The interface is shown to contribute additional scattering in (a) the total scattering, and (b) the backwards scattering direction (away from the glass). The differences shown in having a glass interface versus just water (no interface) suggests that index matching the substrate with the surrounding medium will produce more accurate results.

Video S1. The current density and displacement current as a function of time for a 360 nm core-satellite structure excited by a continuous source azimuthal beam at a wavelength of 700 nm (corresponding to the magnetic dipole mode). Significant displacement currents are found in the gaps between silver nanoparticles, which drives a net circular displacement current around the ring of nanoparticles. The color map indicates the magnitude of the current and displacement current density, and the arrows indicate their polarization.

References

1. Stalder, M.; Schadt, M. *Opt. Lett.* **1996,** 21, (23), 1948-1950.
2. Qian, Z. X.; Hastings, S. P.; Li, C.; Edward, B.; McGinn, C. K.; Engheta, N.; Fakhraai, Z.; Park, S. J. *ACS Nano* **2015,** 9, (2), 1263-1270.
3. Sheikholeslami, S. N.; Alaeian, H.; Koh, A. L.; Dionne, J. A. *Nano Lett.* **2013,** 13, (9), 4137-4141.
4. Li, J.; Engheta, N. *Phys. Rev. B* **2006,** 74, 115125.